Simultaneous Bilateral T_1, T_2, and $T_{1\rho}$ Relaxation Mapping of Hip Joint With 3D-MRI Fingerprinting

Anmol Monga, MS,[1*] Hector Lise de Moura, PhD,[1] Marcelo V.W. Zibetti, PhD,[1] Thomas Youm, MD,[2] Jonathan Samuels, MD,[3] and Ravinder R. Regatte, PhD[1]

Background: Three-dimensional MR fingerprinting (3D-MRF) has been increasingly used to assess cartilage degeneration, particularly in the knee joint, by looking into multiple relaxation parameters. A comparable 3D-MRF approach can be adapted to assess cartilage degeneration for the hip joint, with changes to accommodate specific challenges of hip joint imaging.
Purpose: To demonstrate the feasibility and repeatability of 3D-MRF in the bilateral hip jointly we map proton density (PD), T_1, T_2, $T_{1\rho}$, and ΔB_{1+} in clinically feasible scan times.
Study Type: Prospective.
Subjects: Eight healthy subjects, three patients with mild osteoarthritis (OA), and one of the OA patients had femoral acetabular impingement (FAI). A National Institute of Standards and Technology/International Society for Magnetic Resonance in Medicine (NIST/ISMRM) system phantom was also used.
Field Strength/Sequence: 3 T, 3D-MRF sequence for bilateral hip joint mapping. Reference sequences include Volume Interpolated Breath-hold Examination (VIBE) for T_1 mapping, and magnetization-prepared fast low-angle shot (TFL) for T_2 and $T_{1\rho}$ mapping.
Assessment: The signal-to-noise ratio (SNR), repeatability, scan time, and accuracy of T_1, T_2, and $T_{1\rho}$ maps of 3D-MRF sequence were evaluated on a NIST/ISMRM phantom and human subjects. Differences in the parametric maps between OA and healthy subjects were assessed.
Statistical Tests: Regression, Bland–Altman, Kruskal–Wallis, and Wilcoxon tests were used to assess for accuracy, repeatability, and subregional variation. The *P*-value <0.05 indicated statistically significant.
Results: A 3D-MRF sequence sensitive to PD, T_1, T_2, $T_{1\rho}$, and ΔB_{1+} within 15 minutes, achieving high SNR and low test–retest coefficient of variance (T_1: 3.36%, T_2: 3.99%, $T_{1\rho}$: 5.93%). Mild hip OA patients, including one with mild OA and FAI, showed elevation of 29.4 ± 9% (T_2) and 32.4 ± 4.4% ($T_{1\rho}$) in femoral lateral compartment of the hip joint compared to healthy controls.
Data Conclusion: 3D-MRF may be a feasible approach for simultaneous, quantitative mapping of bilateral hip joint cartilage in healthy and mild OA patients.
Evidence Level: 1
Technical Efficacy: Stage 1

J. MAGN. RESON. IMAGING 2024.

The hip joint plays an important role in facilitating the force and load transmission from the axial skeleton to the lower extremities while maintaining the mobility of the human body. The hip joint is susceptible to numerous pathological conditions that can adversely affect stability including femoroacetabular impingement (FAI),[1] primary or secondary osteoarthritis (OA),[2] and labral tears.[3] These diseases are associated with the degradation of articular cartilage and other joint structures, which ultimately leads to joint failure.[4]

The capacity of the articular cartilage to withstand load is dependent on its structure. Water is the major component of articular cartilage, which comprises 67% to 74% of the

View this article online at wileyonlinelibrary.com. DOI: 10.1002/jmri.29679

Received Oct 8, 2024, Accepted for publication Dec 2, 2024.

*Address reprint requests to: A.M., 660 First Avenue, 4th Floor, New York, NY, USA. E-mail: anmol.monga@nyulangone.org

From the [1]Center of Biomedical Imaging, Department of Radiology, New York University Grossman School of Medicine, New York, New York, USA; [2]Department of Orthopedic Surgery, New York University Grossman School of Medicine, New York, New York, USA; and [3]Department of Medicine, Division of Rheumatology, New York University Grossman School of Medicine, New York, New York, USA

total weight of the tissue and functions to help dissipate load across the surface of the bone.[5] The macromolecular matrix comprises the remaining component of cartilage and consists of collagen fibers (CF) and proteoglycans (PG).[6,7] The CF and PG play a crucial role in trapping water molecules, which provides osmotic pressure and contributes to the tensile and compressive strength of cartilage.[8] The relationship between the various constituents of articular cartilage and their relaxation times, such as spin–lattice relaxation time (T_1), spin–spin relaxation time (T_2), and spin–lattice relaxation time in the rotating frame ($T_{1\rho}$), have been extensively investigated.[5,9,10]

Biomarkers from MRI, including T_1, T_2, and $T_{1\rho}$, can quantify diseases related changes in the composition and structure of articular cartilage.[9,11–16] Specifically, T_1-weighted images or T_1 parametric maps were acquired with Delayed Gadolinium Enhanced MRI of Cartilage (dGEMRIC) using intravenous (IV) injections.[17] The contrast agent administration is sensitive to early-stage cartilage degradation and has been shown to correlate with the PG content.[18] However, the use of contrast agents has certain limitations including the wait time needed for the contrast to penetrate the articular cartilage in the hip, the additional cost, and the potential dangers with kidney and liver diseases.[19] Yet, T_2-weighted images or T_2 parametric maps can be acquired without the use of contrast agents and are sensitive to changes in the CF ultrastructure in the articular cartilage.[20] The relationship between changes in the T_2 with cartilage degradation has been discussed extensively.[9,12,14,21] In this regard, $T_{1\rho}$-weighted images or $T_{1\rho}$ parametric maps can also be acquired without the need for contrast agents and are sensitive to changes in PG content[15] and early cartilage degeneration.[10,16] As such, T_1, T_2, and $T_{1\rho}$ can help to evaluate slightly different constituents of articular cartilage and hence could provide complementary information.[10,22]

The conventional approach for estimating tissue properties from MRI using individual acquisitions of each parametric map results in long scan times and artifacts due to motion. However, MR Fingerprinting (MRF) allows the acquisition of multiple parametric maps simultaneously during a single acquisition and addresses many of the limitations of conventional MRI approaches.[23] There have been several previous publications aimed at exploring the MRF framework in articular cartilage and other musculoskeletal structures, especially in the knee,[24,25] hip,[26,27] and lumbar spine.[28]

The purpose of this study was to demonstrate the feasibility and repeatability of a three-dimensional (3D)-MRF technique in generating T_1, T_2, and $T_{1\rho}$ parametric maps of the bilateral hip joints for healthy subjects and patients with mild hip OA in clinically feasible scan times.

Materials and Methods

This prospective study was approved by the local institutional review board, and all subjects provided written informed consent before research was initiated. This study was performed in compliance with the Health Insurance Portability Act.

3D-MRF Sequence Design and Dictionary Construction

The 3D-MRF sequence quantified five parameters: Proton density (PD), T_1, T_2, and $T_{1\rho}$, and ΔB_{1+}. A single shot of the sequence consisted of three components, as illustrated in Fig. 1a: 1) an adiabatic inversion pulse followed by two fast imaging segments based on steady-state precession (FISP), with 250 excitations each, flip angles (FA) sinusoidally varying from 0° to 20°, and from 0° to 60° for the first and second segments, that was used to encode T_1 and T_2; 2) two fast low-angle shot (FLASH) segments, arranged similarly to the previous two segments, that were used to encode T_1 relaxation time and ΔB_{1+}; and 3) a series of four FLASH segments, with 125 excitations each, with FA sinusoidally varying from 0° to 20°, preceded by a $T_{1\rho}$ preparation module with spin-lock times (TSLs) of 0.50, 4.20, 9.80, and 21.80 msec that were used to encode $T_{1\rho}$ at a spin-lock frequency (FSL) of 400 Hz. Similar TSLs were used to acquire 3D-MRF signals on the knee joint.[29] A self-compensated $T_{1\rho}$ preparation module[30] robust to B_0 and B_1 inhomogeneities was used.

A 3D golden-angle radial stack-of-stars k-space trajectory was used for the MRF acquisition, as shown in Fig. 1. This trajectory used radial readouts with golden angle increments between them in the imaging plane and Cartesian spacing along the slice (kz) direction. The illustration in Fig. 1a corresponds to one shot of the sequence. When more shots are used, the sequence is repeated with readout angles incremented by 180°/N, where N is the number of shots as seen in Fig. 1b. Cartesian phase-encoding steps are performed from the center partition to the k-space periphery (centric out) along the kz direction (Fig. 1c). All shots were acquired within the partition encoding loop and all the 3D-MRF sequence imaging parameters are shown in Fig. 1d. The feasibility of MRF acquisitions of 1, 2, 4, and 8 shots was investigated. The time for acquisition for the proposed MRF sequence with 1, 2, 4, and 8 shots were 3 minutes 42 seconds, 7 minutes 14 seconds, 14 minutes 11 seconds, and 28 minutes 5 seconds, respectively.

The 3D-MRF sequence was acquired on the same 3 T MRI scanner (MAGNETOM Prisma, Siemens Healthcare, Forchheim, Germany) using an 18-channel flexible body coil and parts of a 32-channel spine coil to acquire the bilateral hip joint. The MRF sequence was acquired with the following imaging parameters: repetition time (TR) = 7.5 msec; echo time (TE) = 3.5 msec; receiver bandwidth = 400 Hz/pixel; field of view (FOV) = 300 mm; number of voxels = 432 × 432; slice thickness = 3 mm; number of slices = 14; voxel size = 0.7 mm × 0.7 mm × 3.0 mm.

The 3D-MRF sequence was acquired in both a National Institute of Standards and Technology/ International Society for Magnetic Resonance in Medicine (NIST/ISMRM) system phantom and human subjects. The range of T_1, T_2, and $T_{1\rho}$ values in the phantom were higher than the values in articular cartilage. The MRF dictionary was constructed using fingerprints corresponding to 32 ΔB_{1+} values ranging from 30° to 90° with a 2-degree step size. The maximum FA in the FA train of the MRF sequence was 60°. It was assumed that B_{1+} field caused uniform fluctuation across the FA train. The variation in reference maximum flip angle can be used to model the fluctuations. These fluctuations were modeled in the MRF

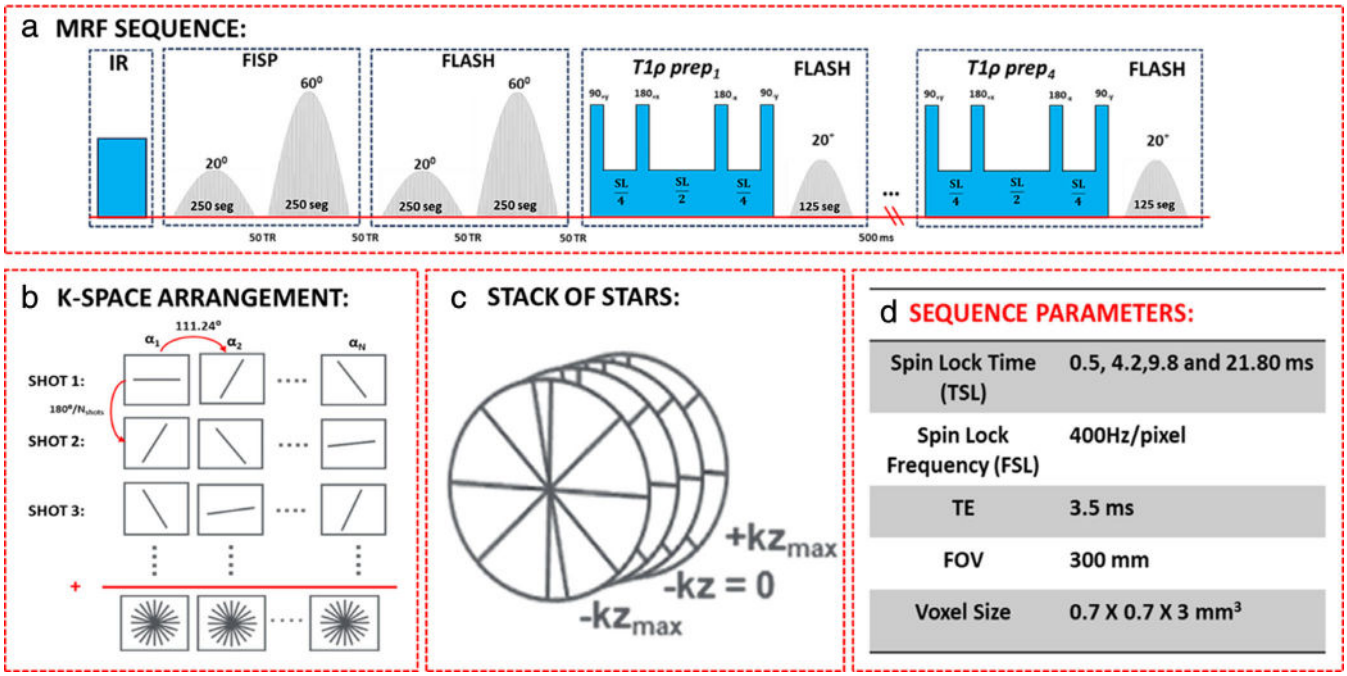

FIGURE 1: (a) 3D-MRF sequence timing diagram. Two FISP and two FLASH segments with 250 RF excitation pulses and radial readouts were used after an adiabatic pulse to encode T_1/T_2 and T_1/B_{1+}. The flip angle varies in a sinusoidal fashion between 0° and 20° in the first segment and between 0° and 60° in the second segment of each FISP or FLASH part. Then four balanced $T_{1\rho}$ preparation modules with different spin-lock durations were applied, followed by FLASH segments with 125 excitations and readout. The flip angle in each segment varied between 0° and 20°. (b) A radial spoke was acquired after each excitation with a golden angle increment. Each shot includes a train of 1500 variable flip angles. To increase the SNR, the train was repeated (second shot) with a 90° offset and summed to generate a radial k-space trajectory per slice. A stack of stars was acquired for volumetric coverage. (c) Cartesian phase-encoding steps are performed from the center partition to the k-space periphery (centric out) along the kz direction. (d) 3D-MRF sequence imaging parameters.

dictionary by varying reference maximum FA from 30° to 90° (i.e., −50% to +50% fluctuation from reference maximum flip angles) with a 2-degree step size while keeping the FA train structure unchanged. The 32 ΔB_{1+} values are used in the MRF dictionary prepared for both NIST/ISMRM system phantom and human subjects.

For the NIST/ISMRM system phantom, the MRF dictionary was prepared using fingerprints with relaxation times 50–3000 msec for T_1, 2–200 msec for T_2, and 2–200 msec for $T_{1\rho}$ with a step size of 7%. In the in-vivo experiment using human subjects, the MRF dictionary is prepared using fingerprints with T_1 ranging from 300 to 2000 msec, T_2, and $T_{1\rho}$ ranging from 15 to 100 msec with a step size of 3%. The fingerprints in the MRF dictionary were simulated using extended phase graphs (EPG).[31] The measured MR fingerprints and simulated dictionary were compressed using singular value decomposition (SVD)[32] to speed up parametric map reconstruction. The T_1, T_2, $T_{1\rho}$, and ΔB_{1+} maps of the bilateral hip were constructed by estimating the best matches between the compressed MR fingerprints from the dictionary and compressed signal evolution for each voxel. The inner product served as the matching criteria, with the best matches corresponding to the highest inner product values. All algorithms were implemented in MATLAB (version R2018b; The MathWorks Inc., Natick, MA, USA).

Conventional T_1, T_2, and $T_{1\rho}$ Mapping

Conventional T_1, T_2, and $T_{1\rho}$ maps of the NIST/ISMRM system phantom and hip cartilage were also acquired for comparison with the MRF sequence. A 3D-Volumetric Interpolated Breath-hold examination (VIBE) sequence was acquired with 10 different FAs, ranging from 1° to 19° in 2° steps to estimate T_1 relaxation time using Siemens inline mapping software (VE11C, Siemens Healthcare, Forchheim, Germany). A $T_{1\rho}$-prepared Turbo-FLASH (TFL) sequence was used to acquire multiple scans with variable TSLs including 0.025, 36, 45, and 45 msec to estimate $T_{1\rho}$ relaxation time with a spin-lock frequency of 400 Hz.[33] The same TFL sequence, called T_2-prepared TFL, was used to acquire multiple scans to estimate T_2 relaxation time.[34] This was done using the same parameters but without a spin-lock pulse applied (i.e., 0 Hz). The FOV of the sequence was 300 mm with a resolution of 0.7 mm × 0.7 mm × 3.0 mm. Cartilage T_2 and $T_{1\rho}$ maps were generated by fitting mono-exponential models using nonlinear least squares (NLS) optimization in MATLAB (version R2022b; The MathWorks Inc., Natick, MA, USA).

NIST/ISMRM System Phantom

The MRF sequence was tested on the NIST/ISMRM system phantom.[35] The NIST/ISMRM system phantom comprised 3-arrays: PD array, Nickel Chloride ($NiCl_2$) array, and Manganese Chloride ($MnCl_2$) array. The tests on the $MnCl_2$ array consisted of 14 spheres containing pure water doped with $MnCl_2$. The $MnCl_2$ doped array spanned a range of relaxation times similar to human tissue. The spheres in the $MnCl_2$ doped arrays in NIST/ISMRM system phantom were segmented manually (A.M; 7 years of medical imaging

experience) and labeled as regions of interest (ROIs) 1–14 as illustrated in Fig. 2a. The region of interest encloses the spheres in $MnCl_2$ array with varying T_1, T_2, and $T_{1\rho}$ values based on the degree of $MnCl_2$ doping in pure water. As we move from ROI1 to ROI14 the values of T_1, T_2, and $T_{1\rho}$ should decrease as shown in supplementary documents attached to Stupic et al.[35] The SNR, mean, standard deviation (SD), and coefficient of variation (CV) across the spheres in the $MnCl_2$ array of the NIST/ISMRM phantom were evaluated to investigate the noise level and standard deviation for 1-, 2-, 4-, and 8-shot MRF acquisition. The mean values estimated by 3D-MRF were compared against the mean values estimated by conventional reference quantitative MRI maps in the spheres of the NIST/ISMRM system phantom.

Healthy Volunteers and Patients With Hip Osteoarthritis

The study group consisted of eight healthy volunteers (mean age = 32 ± 2 years; six males and two females) who had no current or prior history of hip pain, trauma, surgery, osteoarthritis, or inflammatory or crystalline-induced arthritis. We also included three mild hip OA patients (mean age = 56 ± 15 years; two males and one female). The three mild hip OA patients had Kellgren-Lawrence (KL) grades 1 for both hips in patient 1; KL-2 in the right hip joint and KL-1 in the left hip joint in patient 2; and patient 3 had KL-1 for both hips and FAI with cam lesion along with labral tears in both hips. A board-certified musculoskeletal radiologist with 7 years of experience provided imaging diagnosis of OA based on Scoring Hip Osteoarthritis with MRI (SHOMRI) scoring criteria.[36] The 1-, 2-, and 4-shot MRF acquisitions were performed on a single healthy human subject. The mean, SD, and CV of T_1, T_2, and $T_{1\rho}$ maps were calculated along with the SNR for the PD images to determine the best acquisition parameters for the 3D-MRF sequence. The mean T_1, T_2, and $T_{1\rho}$ values were also calculated for the rest of the healthy subjects and patients with hip joint degeneration. These values were compared for changes in T_1, T_2, and $T_{1\rho}$ values in patients with hip joint degeneration to those with healthy hip joints.

Repeatability of Manual Cartilage Segmentation

The ROIs were manually drawn (A.M. 7 years of medical imaging experience) using the Volume Segmenter app with MATLAB (version R2022b; The MathWorks Inc., Natick, MA, USA). The articular cartilage was divided into two layers: femoral and acetabular. The femoral layer was further segmented into four compartments including femur lateral (FL), femur superolateral (FSL), femur superomedial (FSM), and femur inferior medial (FIM). The acetabular layer was subdivided into acetabular superolateral (ASL) and acetabular superomedial (ASM). The articular cartilage was divided based on anatomical direction: inferior and superior, lateral, and medial. The weight-bearing femoral and acetabular cartilage are the primary areas of the hip joint subjected to the majority of load. The weight-

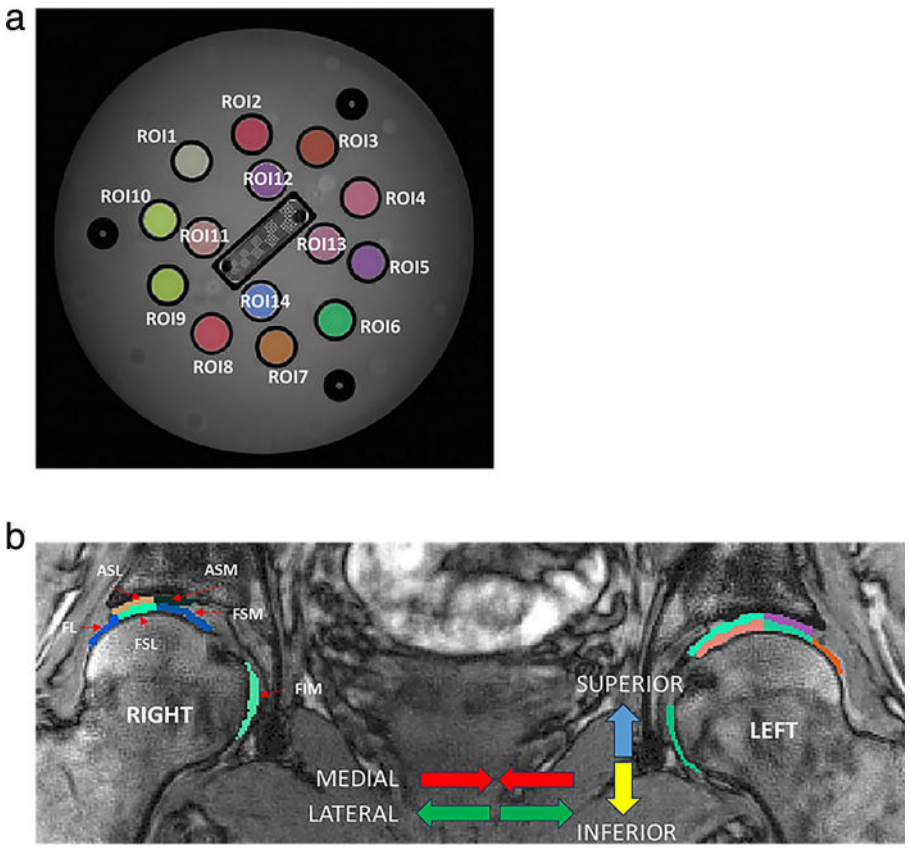

FIGURE 2: Panel (a) highlights the label of spheres in the $MnCl_2$ doped array of the NIST/ISMRM system phantom. Panel (b) highlights the segmentation of bilateral hip joints. The hip joint comprises femoral cartilage (pads of the femoral head) and acetabular cartilage (pads of the acetabulum). Based on the anatomical geometry the cartilages in the hip joint are further divided based on medial-lateral directions and superior–inferior directions. The subregions of the femoral cartilage are FL, FSL, FSM, and FIM. The subregions of the acetabular cartilage are ASL and ASM.

bearing femoral cartilage includes the FL, FSL, and FSM compartments, while the weight-bearing acetabular cartilage consists of the ASL and ASM compartments. Non-weight-bearing femoral cartilage comprises of FIM compartment. A similar method for segmenting the femur and acetabular cartilage of the hip joint was described in Anwander et al.[37]

The PD estimated from the MRF acquisition provided the best anatomical visualization of the femur and acetabular cartilage of the hip. Hence, the cartilage ROIs in MRF images were demarcated using the PD images. The segmentation is illustrated in Fig. 2b.

Eight healthy volunteers were used to analyze the variation in T_1, T_2, and $T_{1\rho}$ values across compartments of femoral and acetabular cartilage of the hip. To evaluate the biochemical changes in cartilage between healthy subjects and OA patients with degenerated hip cartilage, we compared the T_1, T_2, and $T_{1\rho}$ maps estimated from the MRF acquisition for the respective subjects. Specifically, we analyzed the mean T_1, T_2, and $T_{1\rho}$ values in the FL, FSL, FSM, FIM, ASM, and ASL compartments of the articular cartilage in the hip, comparing these values between OA and healthy subjects. To assess the repeatability of the segmentation, manual cartilage segmentations were performed twice (A.M. 7 years of medical imaging experience), with a 3-month interval on 3D-MRF acquisitions from all eight healthy volunteers. The variation in T_1, T_2, and $T_{1\rho}$ values were assessed.

Statistical Analysis

GraphPad Prism software (version 10.3.1; GraphPad Software, Boston, MA, USA) was used to perform the Bland–Altman analysis and regression analysis. The irr package in R studio (version 2023.06.2; posit.co/products/open-source/rstudio/) was used to calculate the intra-class correlation coefficient (ICC) values. MATLAB (version R2022b; The MathWorks Inc., Natick, MA, USA) built-in functions were used to perform Wilcoxon and Kruskal–Wallis test.

Regression analysis was performed between T_1, T_2, and $T_{1\rho}$ parameters estimated from the 3D-MRF acquisition and conventional T_1, T_2, and $T_{1\rho}$ mapping sequences. R^2 values provide the goodness of fit between two quantitative MRI techniques. Bland–Altman analysis was performed to estimate the biases of the MRF acquisition compared to the conventional mapping sequence. This analysis was performed on the spheres of the $MnCl_2$ array of the NIST/ISMRM system phantom.

The Wilcoxon test was used to evaluate differences between the left and right hips; the femoral and acetabular cartilage of the hips. A Kruskal–Wallis test was used to evaluate significant differences between compartments (FL, FSL, FSM, FIM, ASL, and ASM) of femoral and acetabular hip articular cartilage.

The agreement between repeated manual cartilage segmentations in healthy volunteers ($N = 8$) is evaluated using ICC and Bland–Altman analysis. The percentage biases between two repeated measurements and their SD were calculated for T_1, T_2, and $T_{1\rho}$ maps. The intrasubject test–retest MRF repeatability scans in healthy ($N = 2$) and mild hip OA patients ($N = 2$) were assessed by comparing T_1, T_2, and $T_{1\rho}$ values, using the Bland–Altman plots. The coefficient of variation (CV) and bias were also measured to assess the repeatability. A P-value <0.05 was considered statistically significant.

Results

NIST/ISMRM System Phantom

The T_1, T_2, $T_{1\rho}$, and SNR maps for 1-, 2-, 4-, and 8-shot MRF acquisitions in the NIST/ISMRM phantom were visualized in Fig. 3. Table 1 highlights the mean, SD, and SNR for T_1, T_2, and $T_{1\rho}$ in ROI1–14, respectively. The mean T_1, T_2 and $T_{1\rho}$ values for the spheres in the $MnCl_2$ array of the NIST/ISMRM system phantoms increased as we increased the number of shots. The spheres contained water that was doped uniformly with $MnCl_2$. Hence, T_1, T_2, and $T_{1\rho}$ estimated within the spheres should have a low SD. Table 1 showed that as we increased the number of shots in MRF acquisition the SD decreased. In the MRF acquisition with 8 shots, the estimated T_1, T_2, and $T_{1\rho}$ showed the lowest SD. The CV for T_1 ranged from 3.3% in ROI10 to 10.6% in ROI1, the CV for T_2 ranged from 5.3% in ROI4 to 56.7% in ROI14, and the CV for $T_{1\rho}$ ranged from 5.7% in ROI1 to 50.9% in ROI14, respectively. As summarized in Table 1, the SNR increased from 53.83 ± 2.12 to 72.64 ± 2.25 as we increased the number of shots.

The regression and residual plots illustrating the relation between MRF parametric maps and conventional reference parametric maps are shown in Fig. 4. The estimated R^2 values between T_1 parametric maps for the MRF acquisition with 1, 2, 4, and 8 shots and the reference T_1 parametric maps were 0.99, 0.99, 0.99, and 0.99, respectively. The slopes of the regression plot for 1-, 2-, 4-, and 8-shot MRF acquisition were 1.07, 0.90, 0.96, and 0.95, respectively. The percentage biases calculated on T_1 maps from the MRF acquisition compared to the reference scan were 5%, 8.7%, 7.1%, and 7% for 1-, 2-, 4-, and 8-shot acquisition, respectively. The R^2 values describing the relationship between $T_{1\rho}$ estimated from the 1-, 2-, 4-, and 8-shot MRF acquisition and those estimated from the reference $T_{1\rho}$ maps were 0.91, 0.96, 0.99, and 0.99, respectively. The slopes of the regression plot for 1-, 2-, 4-, and 8-shot MRF acquisition were 1.21, 1.28, 1.26, and 1.23, respectively. The percentage biases between $T_{1\rho}$ maps estimated from the MRF acquisition (1, 2, 4, and 8 shots) and those estimated from the reference scan were 34%, 35%, −0.7%, and 4%, respectively. The R^2 values between T_2 estimated from 1-, 2-, 4-, and 8-shot MRF acquisition and those estimated from the reference scans were 0.99, 0.99, 0.99, and 0.99, respectively. The slopes of the regression plot for 1-, 2-, 4-, and 8-shot MRF acquisition were 1.27, 1.29, 1.29, and 1.26, respectively. The percentage biases between T_2 maps estimated from MRF (1, 2, 4, and 8 shots) and those estimated from the reference scan were 5.6%, 6.6%, 6.7%, and 7%, respectively. The regression analysis results were statistically significant. The analysis showed that the biases decreased particularly for $T_{1\rho}$ and R^2 goodness of fit increased with an increase in the number of shots.

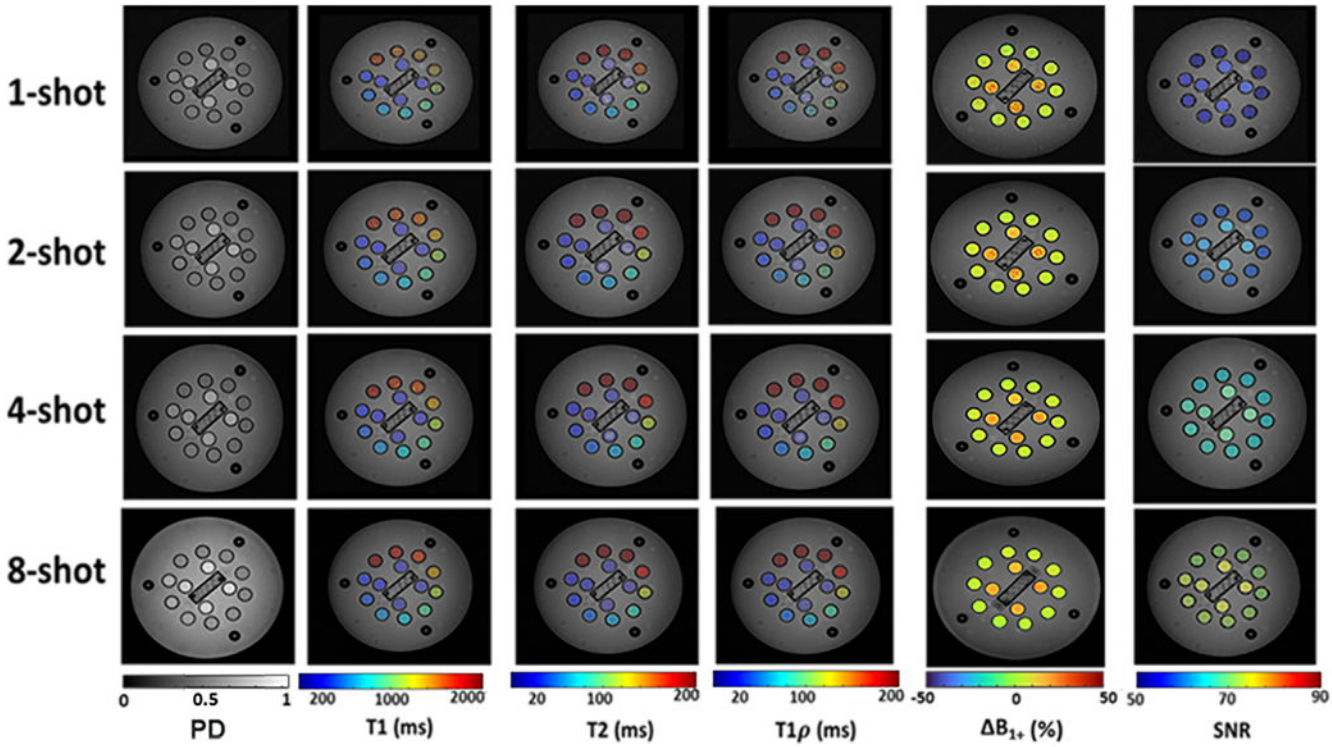

FIGURE 3: The PD, T_1, T_2, $T_{1\rho}$, ΔB_{1+} maps estimated from MRF acquisition of ROI1–14 in the NIST/ISMRM system phantom. As we move from ROI1 to ROI14, the T_1, T_2, and $T_{1\rho}$ values decrease consistently. The standard deviation in the T_1, T_2, and $T_{1\rho}$ values decreases with increase in number of shots. The SNR within the spheres of the phantom increases with the number of shots.

The acquisition time for 1-, 2-, 4-, and 8-shot MRF were 3 minutes 42 seconds, 7 minutes 14 seconds, 14 minutes 11 seconds, and 28 minutes 5 seconds, respectively. The acquisition time for MRF increased with an increase in the number of shots while improving accuracy and decreasing variation due to noise.

Healthy Volunteers and Patients With Hip Osteoarthritis

In Table 2, T_1, T_2, and $T_{1\rho}$ relaxation times are shown for weight-bearing femoral cartilage, weight-bearing acetabular cartilage, and non-weight-bearing femoral cartilage, thus combining multiple compartments. As shown in Table 2, the SNR of the acquisition improved significantly from 9.37 ± 1.9 to 21.15 ± 1.9 by increasing the number of shots from 1 to 4. The CV of T_1 relaxation time in the hip joint significantly decreased from 60.7% to 36.8% by increasing the number of shots from 1 to 4. However, the CV remained constant for T_2 and $T_{1\rho}$ relaxation times. In the femoral cartilage, the CV of T_2 and $T_{1\rho}$ maps decreased with the number of shots. The CV of T_2 and $T_{1\rho}$ maps remained constant in acetabular cartilage while for T_1 maps CV decreased. The SD for estimated T_1, T_2, and $T_{1\rho}$ maps estimated from MRF acquisition showed a gradual decrease with the number of shots. Figure 5 illustrates the representative T_1, T_2, and $T_{1\rho}$ relaxation time maps in the hip joints.

The precision of ICC in the bilateral hip manual cartilage segmentation for T_1, T_2, and $T_{1\rho}$ values, were 0.92, 0.90, and 0.93, respectively. Figure 6a–c shows the scatter plots with the X-axis as relaxation times from the original manual segmentation and the Y-axis as the relaxation time of repeated segmentations. The Bland–Altman plots in Fig. 6a–c illustrate the percentage biases and variance in relaxation times between the repeated manual segmentations, with percentage biases of 1.15% for T_1, −1.32% for T_2, and −1.23% for $T_{1\rho}$.

The Bland–Altman plots for test–retest repeatability are illustrated in Fig. 6d–f. The intrasubject CV between two repeated acquisitions for T_1, T_2, and $T_{1\rho}$ maps were 3.36%, 3.99%, and 5.93%, respectively. The biases between the test and retest for T_1, T_2, and $T_{1\rho}$ were −20.15, 0.396, and 1.44 msec, respectively. The percentage biases between test and retest for T_1, T_2, and $T_{1\rho}$ were −3.9%, 0.19%, and 5.5%, respectively.

The T_1, T_2, and $T_{1\rho}$ showed no significant difference between the left and right hip joints (P-values: $T_1 = 0.104$; $T_2 = 0.970$; $T_{1\rho} = 0.307$) or between the femur and acetabular cartilage (P-values: $T_1 = 0.850$; $T_2 = 0.162$; $T_{1\rho} = 0.186$). The Kruskal–Wallis test showed significant variation in the subregions (FL, FSL, FSM, FIM, ASL, and ASM) for T_1, T_2, and $T_{1\rho}$ maps. The box plots in Fig. 7 illustrate the variation in the MRF parametric maps. The T_1 values in FIM, FL, and FSL were 19% higher than values in

TABLE 1. Mean, SD, and Coefficient of Variation (CV) for T_1, T_2, and $T_{1\rho}$ Values on Regions of Interest of the NIST/ISMRM System Phantom

Shots	Subregions	T_1	T_2	$T_{1\rho}$	SNR
1 Shot	ROI-1	2352.4 ± 1290.4 (54.9%)	389.9 ± 66.8 (17.1%)	399.5 ± 64.6 (16.2%)	53.83
	ROI-2	1907.1 ± 1051.7 (55.1%)	333.1 ± 79.6 (23.9%)	355.3 ± 84.9 (23.9%)	
	ROI-3	1912.9 ± 1252.2 (65.5%)	267.0 ± 75.2 (28.2%)	317.1 ± 100.8 (31.8%)	
	ROI-4	1557.7 ± 957.0 (61.4%)	193.6 ± 54.7 (28.3%)	271.9 ± 123.4 (45.4%)	
	ROI-5	1215.4 ± 419.0 (34.5%)	125.7 ± 27.0 (21.5%)	234.7 ± 148.5 (63.3%)	
	ROI-6	948.9 ± 226.2 (23.8%)	87.8 ± 15.8 (18.0%)	182.0 ± 144.9 (79.6%)	
	ROI-7	733.4 ± 162.7 (22.2%)	62.9 ± 11.9 (18.9%)	125.1 ± 121.6 (97.2%)	
	ROI-8	585.7 ± 159.5 (27.2%)	45.3 ± 10.5 (23.1%)	89.0 ± 100.2 (112.6%)	
	ROI-9	428.9 ± 101.7 (23.7%)	32.7 ± 7.5 (23.0%)	52.8 ± 59.0 (111.6%)	
	ROI-10	310.2 ± 57.3 (18.5%)	23.1 ± 6.5 (28.1%)	33.3 ± 28.5 (85.8%)	
	ROI-11	218.4 ± 42.2 (19.3%)	15.4 ± 5.6 (36.5%)	20.8 ± 15.4 (73.7%)	
	ROI-12	138.5 ± 32.4 (23.4%)	8.8 ± 4.6 (52.0%)	14.2 ± 15.9 (112.3%)	
	ROI-13	114.8 ± 31.7 (27.6%)	7.1 ± 4.0 (57.0%)	14.4 ± 24.7 (172.0%)	
	ROI-14	89.7 ± 27.0 (30.1%)	5.7 ± 4.3 (74.9%)	13.4 ± 23.4 (174.4%)	
2 Shot	ROI-1	1995.9 ± 427.2 (21.4%)	407.5 ± 35.6 (8.7%)	409.0 ± 35.2 (8.6%)	59.89
	ROI-2	1738.6 ± 340.3 (19.6%)	326.0 ± 32.5 (10.0%)	339.0 ± 45.1 (13.3%)	
	ROI-3	1601.6 ± 278.0 (17.4%)	262.2 ± 26.7 (10.2%)	296.5 ± 71.2 (24.0%)	
	ROI-4	1382.2 ± 209.2 (15.1%)	189.3 ± 16.8 (8.9%)	255.3 ± 107.2 (42.0%)	
	ROI-5	1126.9 ± 125.4 (11.1%)	125.2 ± 10.9 (8.7%)	196.9 ± 118.1 (60.0%)	
	ROI-6	912.8 ± 85.0 (9.3%)	87.9 ± 9.6 (11.0%)	132.6 ± 94.0 (70.9%)	
	ROI-7	716.0 ± 58.3 (8.1%)	62.1 ± 8.8 (14.1%)	84.3 ± 57.5 (68.2%)	
	ROI-8	556.0 ± 49.2 (8.9%)	43.7 ± 7.6 (17.5%)	56.2 ± 37.3 (66.4%)	
	ROI-9	415.5 ± 31.3 (7.5%)	31.3 ± 5.5 (17.6%)	37.4 ± 15.3 (40.9%)	
	ROI-10	304.8 ± 23.9 (7.8%)	22.7 ± 4.8 (21.1%)	26.3 ± 10.1 (38.4%)	
	ROI-11	217.1 ± 16.2 (7.5%)	15.6 ± 4.3 (27.7%)	18.5 ± 11.5 (62.4%)	
	ROI-12	136.0 ± 14.8 (10.9%)	9.3 ± 3.4 (36.7%)	11.5 ± 7.1 (61.8%)	
	ROI-13	112.5 ± 14.5 (12.9%)	7.4 ± 3.0 (40.8%)	11.3 ± 12.5 (110.9%)	
	ROI-14	86.2 ± 14.2 (16.5%)	5.8 ± 3.9 (66.6%)	9.0 ± 9.6 (106.2%)	
4 Shot	ROI-1	2143.0 ± 659.3 (30.8%)	409.5 ± 27.0 (6.6%)	409.5 ± 27.0 (6.6%)	66.33
	ROI-2	1802.6 ± 276.5 (15.3%)	320.6 ± 22.5 (7.0%)	321.3 ± 23.9 (7.4%)	
	ROI-3	1644.1 ± 179.3 (10.9%)	258.8 ± 17.4 (6.7%)	264.6 ± 36.5 (13.8%)	
	ROI-4	1414.6 ± 124.4 (8.8%)	186.2 ± 12.1 (6.5%)	208.6 ± 64.3 (30.8%)	
	ROI-5	1140.4 ± 78.1 (6.8%)	122.9 ± 8.6 (7.0%)	144.1 ± 52.5 (36.5%)	
	ROI-6	915.3 ± 50.6 (5.5%)	86.6 ± 8.2 (9.5%)	98.8 ± 30.8 (31.2%)	
	ROI-7	721.2 ± 38.0 (5.3%)	61.8 ± 7.7 (12.5%)	67.4 ± 16.7 (24.7%)	
	ROI-8	557.2 ± 26.9 (4.8%)	44.2 ± 6.6 (14.9%)	47.4 ± 7.6 (16.0%)	
	ROI-9	414.9 ± 19.7 (4.8%)	32.3 ± 4.8 (14.9%)	34.1 ± 6.5 (19.1%)	

TABLE 1. Continued

Shots	Subregions	T_1	T_2	$T_{1\rho}$	SNR
	ROI-10	304.7 ± 12.5 (4.1%)	23.4 ± 4.3 (18.2%)	24.2 ± 3.8 (15.6%)	
	ROI-11	216.0 ± 9.8 (4.6%)	15.6 ± 3.9 (25.1%)	16.4 ± 3.3 (20.2%)	
	ROI-12	135.7 ± 7.8 (5.8%)	9.3 ± 2.9 (30.7%)	10.0 ± 2.6 (26.4%)	
	ROI-13	111.6 ± 7.5 (6.7%)	7.2 ± 2.6 (36.7%)	7.9 ± 2.6 (33.3%)	
	ROI-14	85.0 ± 9.0 (10.5%)	5.7 ± 3.6 (62.6%)	6.6 ± 4.0 (60.2%)	
8 Shot	ROI-1	2101.5 ± 223.1 (10.6%)	404.4 ± 25.3 (6.3%)	405.5 ± 23.2 (5.7%)	72.63
	ROI-2	1831.3 ± 159.0 (8.7%)	309.4 ± 19.0 (6.2%)	310.3 ± 21.3 (6.9%)	
	ROI-3	1651.8 ± 107.6 (6.5%)	254.0 ± 15.9 (6.3%)	255.1 ± 19.7 (7.7%)	
	ROI-4	1411.7 ± 81.9 (5.8%)	184.5 ± 9.9 (5.3%)	189.1 ± 26.5 (14.0%)	
	ROI-5	1141.0 ± 57.3 (5.0%)	123.5 ± 8.2 (6.6%)	130.7 ± 21.0 (16.1%)	
	ROI-6	919.1 ± 41.4 (4.5%)	87.2 ± 9.1 (10.4%)	92.0 ± 20.5 (22.2%)	
	ROI-7	720.6 ± 28.4 (3.9%)	62.7 ± 8.7 (13.9%)	65.0 ± 7.9 (12.1%)	
	ROI-8	560.1 ± 19.3 (3.4%)	44.3 ± 7.5 (16.9%)	46.2 ± 5.7 (12.4%)	
	ROI-9	417.0 ± 15.1 (3.6%)	31.0 ± 5.6 (18.0%)	32.5 ± 4.0 (12.3%)	
	ROI-10	304.9 ± 10.1 (3.3%)	21.9 ± 4.3 (19.7%)	22.8 ± 3.1 (13.8%)	
	ROI-11	215.6 ± 7.5 (3.5%)	15.5 ± 4.1 (26.3%)	16.2 ± 3.0 (18.7%)	
	ROI-12	135.2 ± 5.6 (4.2%)	9.3 ± 3.4 (36.5%)	10.1 ± 2.6 (25.8%)	
	ROI-13	110.8 ± 4.9 (4.4%)	8.1 ± 2.5 (31.3%)	8.3 ± 2.4 (28.5%)	
	ROI-14	83.9 ± 7.1 (8.5%)	6.5 ± 3.7 (56.7%)	6.8 ± 3.5 (50.9%)	

SNR of each shot is also shown. SNR = signal-to-noise ratio; SD = standard deviation; ROI = region of interest; NIST/ISMRM = National Institute of Standards and Technology/International Society for Magnetic Resonance in Medicine.

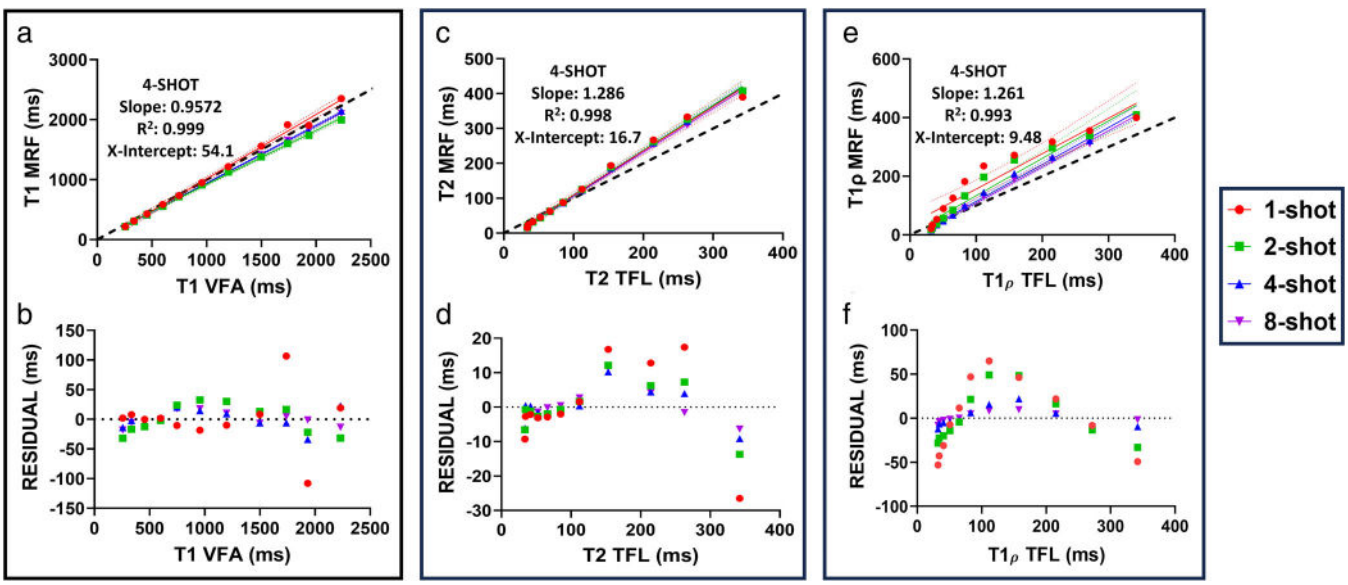

FIGURE 4: Comparing the T_1, T_2, and $T_{1\rho}$ estimated from MRF sequence and conventional MR approaches on a NIST/ISMRM system phantom. The comparison is illustrated by regression plots (a), (c), and (e) and residual plots (b), (d), and (f) for T_1, T_2, and $T_{1\rho}$, respectively. The dashed black line is the identity line in the linear regression plot. Regression and residual plots show a good agreement between the proposed MRF technique and conventional MR approaches. The regression analysis result for the 4-shot MRF acquisition is listed within the plots for T_1, T_2, and $T_{1\rho}$ maps, respectively.

TABLE 2. The Table Illustrates the Mean, SD, and CV for T_1, T_2, and $T_{1\rho}$ Values Across 1-, 2-, and 4-Shot MRF Acquisition of the Bilateral Hip

			Femoral Cartilage						Acetabular Cartilage		
			Weight Bearing			Non-Weight Bearing					
Shots	SNR	Hip Side	T_1 [msec] (CV)	T_2 [msec] (CV)	$T_{1\rho}$ [msec] (CV)	T_1 [msec] (CV)	T_2 [msec] (CV)	$T_{1\rho}$ [msec] (CV)	T_1 [msec] (CV)	T_2 [msec] (CV)	$T_{1\rho}$ [msec] (CV)
1	9.37	Right	734.9 ± 411.9 (56.0%)	32.5 ± 16.6 (51.2%)	52.9 ± 31.6 (59.6%)	720.3 ± 487.2 (67.6%)	31.4 ± 17.8 (56.7%)	58.3 ± 33.7 (57.8%)	839.5 ± 484.0 (57.7%)	39.5 ± 25.9 (65.7%)	60.1 ± 33.4 (55.6%)
		Left	802.4 ± 439.0 (54.7%)	30.4 ± 14.7 (48.3%)	52.6 ± 31.2 (59.3%)	743.5 ± 428.5 (57.6%)	32.2 ± 18.8 (58.3%)	51.8 ± 32.6 (63.0%)	837.6 ± 470.9 (56.2%)	36.4 ± 21.0 (57.9%)	57.6 ± 32.2 (56.0%)
2	14.95	Right	814.4 ± 362.7 (44.5%)	27.3 ± 12.6 (46.1%)	46.0 ± 28.3 (61.6%)	731.7 ± 373.5 (51.1%)	31.4 ± 15.9 (50.8%)	50.9 ± 29.8 (58.6%)	973.7 ± 442.0 (45.4%)	37.0 ± 22.1 (59.7%)	54.1 ± 30.5 (56.4%)
		Left	856.5 ± 341.8 (39.9%)	31.1 ± 12.3 (39.7%)	44.9 ± 25.1 (55.8%)	800.4 ± 388.7 (48.6%)	27.2 ± 13.4 (49.2%)	45.5 ± 29.7 (65.2%)	896.2 ± 410.9 (45.9%)	36.4 ± 20.3 (55.7%)	51.8 ± 30.0 (57.9%)
4	21.15	Right	897.7 ± 285.5 (31.8%)	26.8 ± 8.5 (31.9%)	38.6 ± 21.5 (55.6%)	812.7 ± 323.0 (39.7%)	26.4 ± 10.4 (39.3%)	42.4 ± 27.3 (64.3%)	1029.9 ± 400.3 (38.9%)	35.1 ± 22.3 (63.3%)	45.9 ± 28.3 (61.8%)
		Left	910.0 ± 274.5 (30.2%)	27.7 ± 9.0 (32.5%)	38.3 ± 21.1 (55.1%)	995.8 ± 386.8 (38.8%)	26.1 ± 11.1 (42.3%)	40.1 ± 23.8 (59.4%)	1021.3 ± 358.3 (35.1%)	34.2 ± 20.8 (61.0%)	44.7 ± 26.9 (60.3%)

The relaxation time values are measured for weight-bearing and non-weight-bearing regions of femoral cartilage as well as the acetabular cartilage. The SNR of the acquired MRF is also illustrated for 1-, 2-, and 4-shot MRF acquisitions. SNR = signal-to-noise ratio; SD = standard deviation; MRF = magnetic resonance fingerprinting; CV = coefficient of variation.

FSM and ASL subregions. The T_2 and $T_{1\rho}$ values in the ASM were 22% and 20% higher than the global average, respectively.

The average cartilage T_1, T_2, and $T_{1\rho}$ relaxation times estimated by the proposed MRF acquisition across healthy subjects were 854 ± 93, 27 ± 1.3, and 39 ± 4.8 msec, respectively. For subjects with degenerated cartilage in the hip joint the average T_1, T_2, and $T_{1\rho}$ relaxation times were 854 ± 58, 30 ± 0.2, and 45 ± 3.3 msec, respectively. The differences in the T_1, T_2, and $T_{1\rho}$ values for patients with degenerated hip cartilage and healthy subjects were visible in the subregions of the hip (FL, FSL, FSM, FIM, ASL, and ASM). The variation in T_1, T_2, and $T_{1\rho}$ values between healthy and degenerated hip cartilage across its compartment is illustrated in Fig. 8a–c. The FL compartment in degenerated hip cartilage showed $29.4 \pm 9\%$, and $32.4 \pm 4.4\%$ higher T_2 and $T_{1\rho}$ values compared to healthy controls. In the FIM compartment of the degenerated hip cartilage, $T_{1\rho}$ was elevated by $15.4 \pm 11\%$ compared to healthy controls. In patients with mild OA with KL >1, the $T_{1\rho}$ in the FIM compartment was elevated by $21.5 \pm 4\%$ compared to the healthy controls. Figure 8d provides a representative comparison of T_1, T_2, and $T_{1\rho}$ maps for mild hip OA and healthy articular hip cartilage.

Discussion

We demonstrate that the SNR and scan-time of 3D-MRF on NIST/ISMRM system phantom increased while the CV decreased with an increase in number of shots. The 8-shot 3D-MRF has an SNR of 72.7 with a scan time of 28 minutes 5 seconds. The next best 4-shot 3D-MRF has an SNR of 66.3 with a clinically feasible scan time of 14 minutes 11 seconds. 4-shot 3D-MRF was used on human subjects because it accounts for both high SNR and clinically optimal scan time. The parametric maps T_1, T_2, and $T_{1\rho}$ show 3.36%, 3.99%, and 5.93% CV between repetition for test–retest repeatability analysis for all datasets. The average T_1, T_2, and $T_{1\rho}$ values across healthy subjects are 854 ± 93, 27 ± 1.3, and 39 ± 4.8 msec. The FL compartment of the hip joint has the highest T_1 value compared to other compartments of the hip joint. ASM compartment has the highest T_2 and $T_{1\rho}$ compared to other compartments of the hip joints. The T_2 and $T_{1\rho}$ values in the FL and FIM compartments of hip articular cartilage may be elevated in patients with hip cartilage pathology compared to healthy volunteers, highlighting the potential of MRF-based T_2 and $T_{1\rho}$ maps for detecting early hip cartilage damage.

The values and trends stated above agree with the results of previous studies.[26,27,38,39] The repeatability test showed a slightly higher CV compared to values estimated in previous work[26,27] for T_1, T_2, and $T_{1\rho}$, respectively. Similar

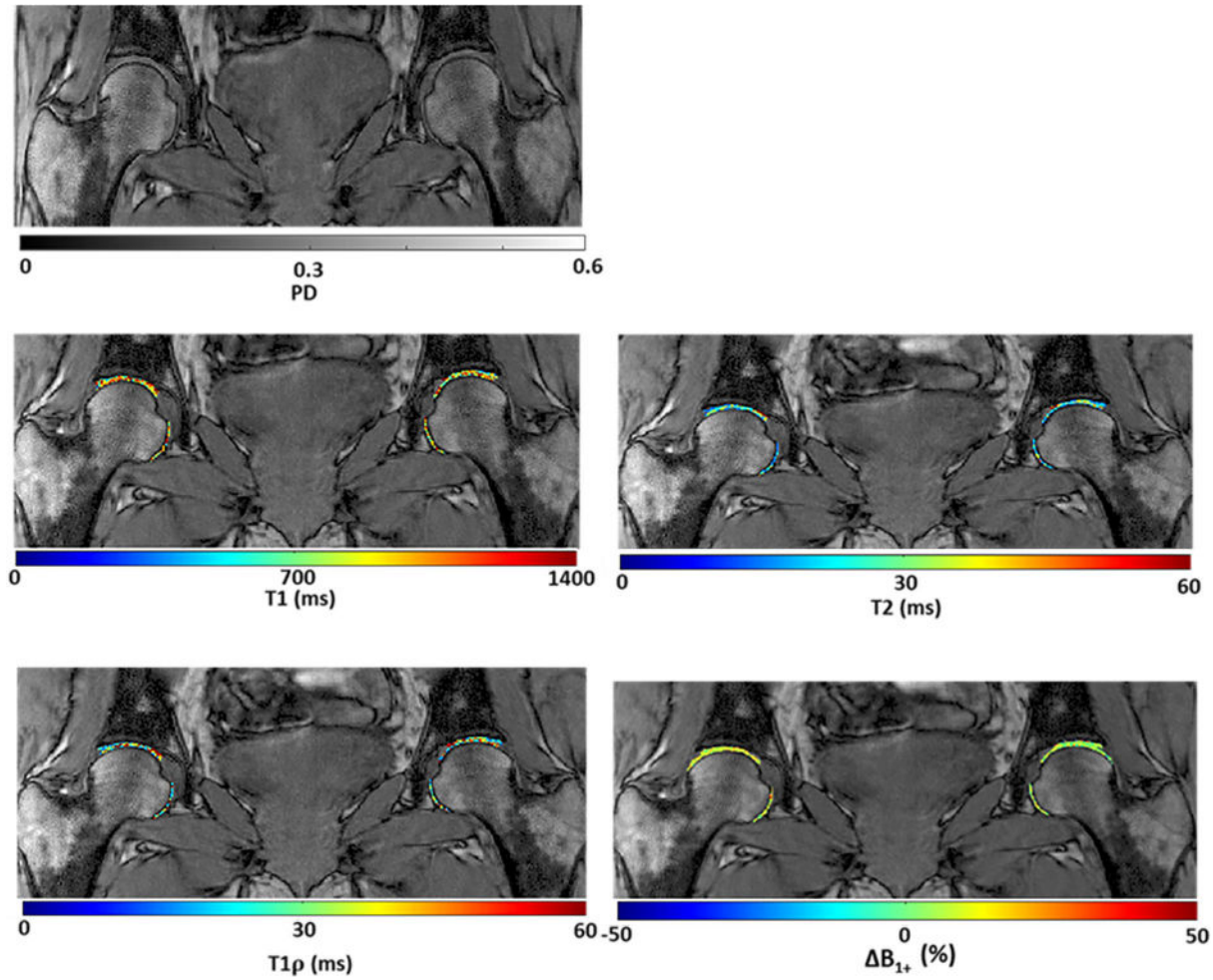

FIGURE 5: Illustrates the representative PD, T_1, T_2, $T_{1\rho}$, and ΔB_{1+} parametric maps in the hip joints.

variation in T_1, T_2, and $T_{1\rho}$ values across compartments of the hip joint in this study can also be seen in Sharafi et al.[27]

The unilateral hip cartilage T_2 and $T_{1\rho}$ maps using a series of weighted images with 4 spin-lock times or echo times were acquired in 13:40 minutes of scan time with a resolution of 0.5 mm × 0.5 mm × 4 mm in Wyatt et al.[38] Unilateral hip T_1 maps were acquired in 1.12 minute per slice using the sequence proposed in Lattanzi et al.[17] Combining all unilateral sequences in a single scan protocol could take 35 minutes to acquire all multiparametric maps. Bilateral hip T_1 and T_2 maps were simultaneously acquired in 7:13 minutes with a resolution of 0.6 mm × 0.6 mm × 4 mm using the MRF sequence proposed in Cloos et al.[26] Bilateral hip T_1, T_2, PD, $T_{1\rho}$, and ΔB_{1+} maps were acquired in 21.18 minutes (only covered six slices; 3.53 minutes per slice) with a resolution of 0.7 mm × 0.7 mm × 4 mm using 2D-MRF sequence proposed in Sharafi et al.[27] In this study, the T_1, T_2, PD, $T_{1\rho}$, and ΔB_{1+} maps were acquired simultaneously with a scan time of 14:11 minutes (14 slices covered the left and right hip joint; 1.02 minute per slice) for a resolution of 0.7 mm × 0.7 mm × 3 mm. The proposed 3D-MRF sequence with simultaneous measurement eliminates the need for co-registration of images and maps. The scan time achieved here, even though incrementally better than what was reported before, is not ideal yet. We believe that optimization of the 3D-MRF pulse sequence can help to reduce scan time in order to reduce the chance of motion and improve patient comfort.

Limitations

The lack of fat saturation pulse in the 3D-MRF sequence is a major limitation of the paper. It can introduce chemical shift artifacts around tissues comprising of fat. In the hip joint region, there are several voxels with high fat content like bone marrow, and fat pad surrounding the acetabular fossa. We use a relatively high receiver bandwidth of 400 Hz/px which mitigates some of the effects of fat around the hip joint. However, high receiver bandwidth leads to lower SNR for MRF acquisition. In the future, we plan to study the use of fat-saturation pulse in MRF acquisition.

The relatively small size of the subject cohort is a major limitation of the study and a larger OA sample size will

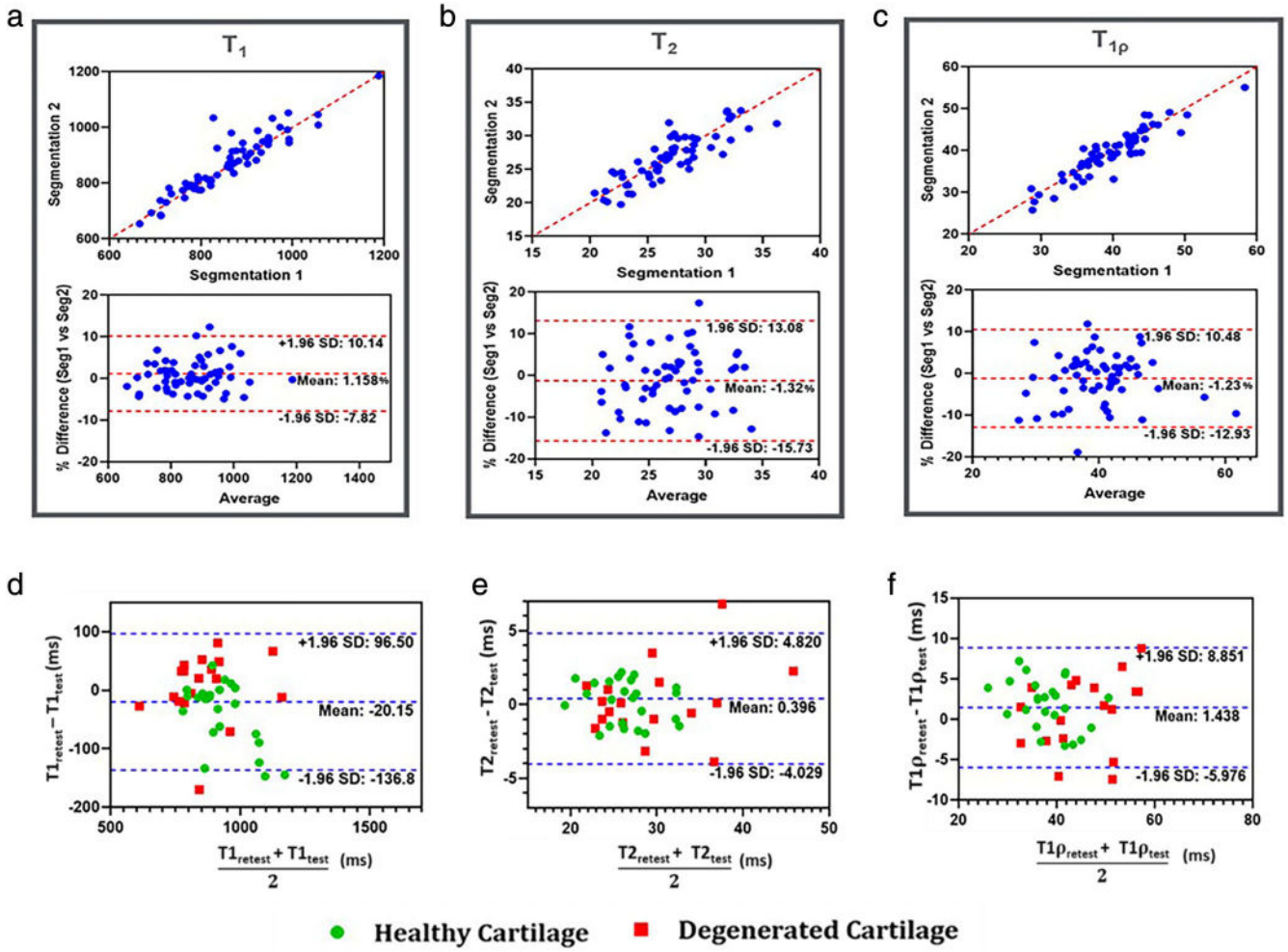

FIGURE 6: Panel (a) shows a scatter plot comparing T_1 values from manual segmentation 1 (X-axis) and manual segmentation 2 (Y-axis), along with a Bland–Altman plot showing the percentage difference in T_1, T_2, and $T_{1\rho}$ values between the two segmentations relative to the average T_1 values. Panels (b) and (c) present similar plots for T_2 and $T_{1\rho}$, respectively. Panels (d), (e), and (f) illustrate the Bland–Altman plot assessing test–retest repeatability of T_1, T_2, and $T_{1\rho}$ values from the proposed 3D-MRF acquisition in both healthy volunteers and patients with hip joint degeneration.

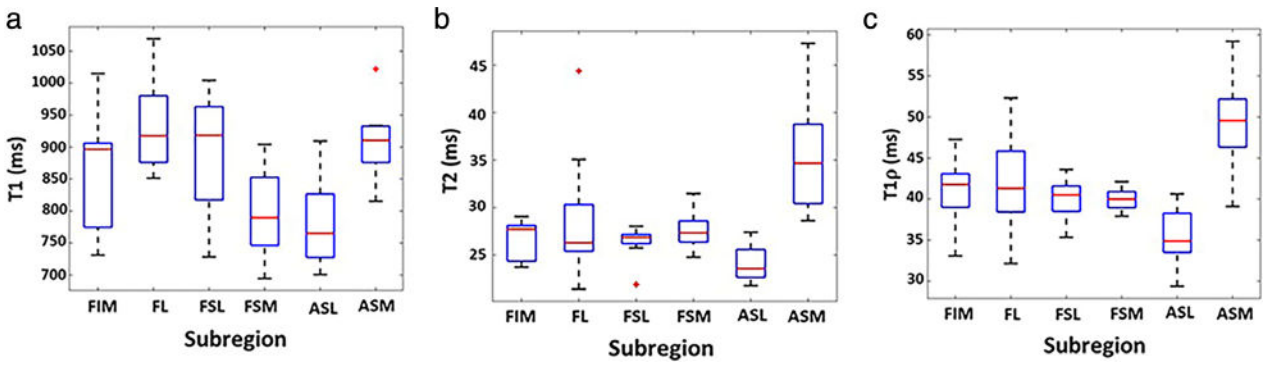

FIGURE 7: Panels (a), (b), and (c) illustrate box plots of T_1, T_2, and $T_{1\rho}$ relaxation time across the subregions of articular cartilage of the hip joint. Kruskal–Wallis test shows a significant separability between the anatomical subregions of the hip joint.

improve the robustness and generalization of results. The repeatability analysis of 3D-MRF acquisition is limited to a single site and vendor. In a future study, we plan to run a reproducibility study across multiple scanners and different sites.

The dictionary matching and MRF reconstruction algorithms used in this study were inefficient in terms of memory requirements and computational speed. Deep learning has been extensively used in MRF and could help in decreasing the speed and memory requirement of MRF

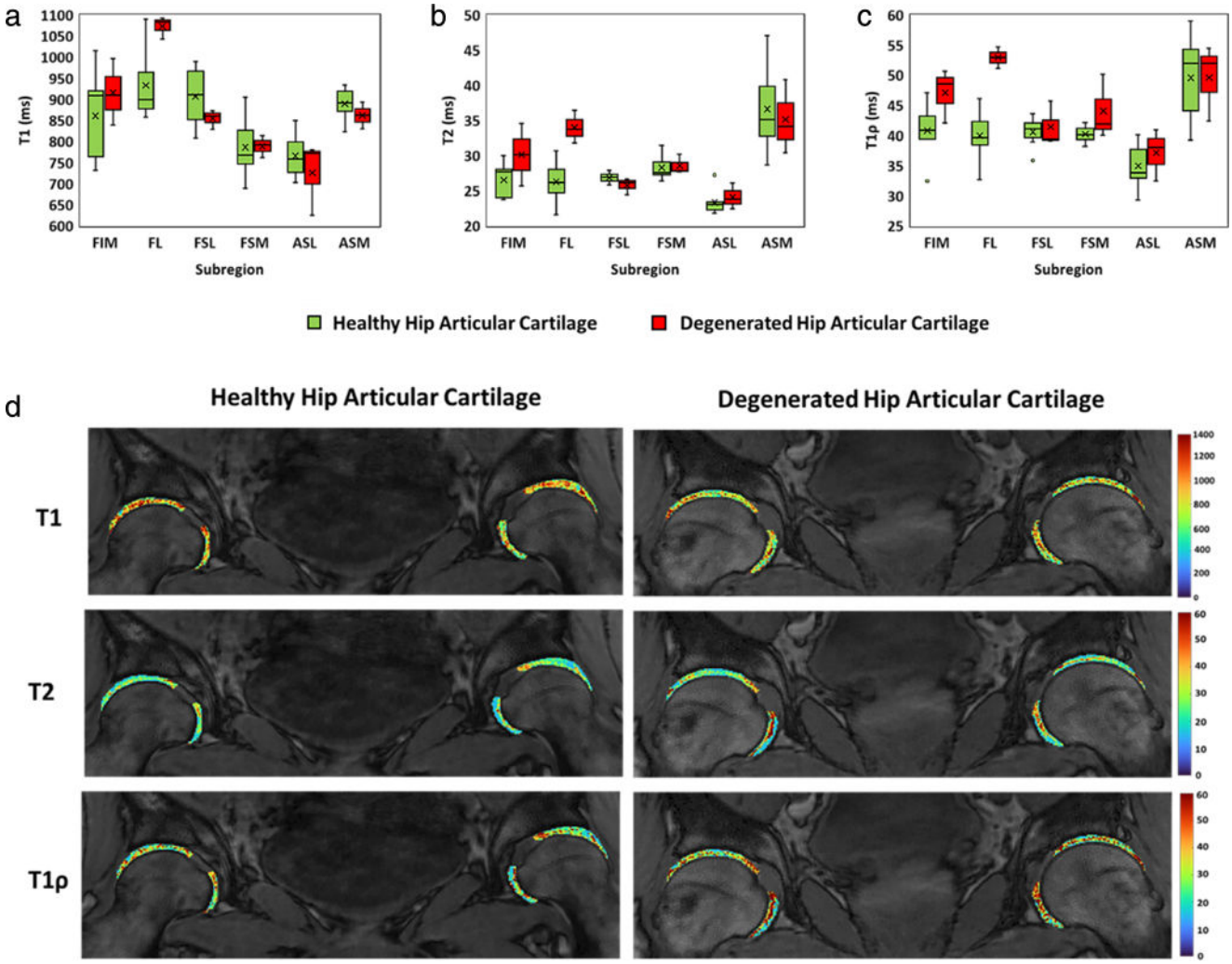

FIGURE 8: Panels (a), (b), and (c) illustrate box plots of T_1, T_2, and $T_{1\rho}$ relaxation time for degenerated and healthy articular hip cartilage across its subregions. Panel (d) illustrates the representative comparison for T_1, T_2, and $T_{1\rho}$ parametric maps for healthy and degenerated articular hip cartilage. The parametric maps are not generated in the acetabular fossa and ligament region. An example of a subject with mild OA, with signs visible in both the right and left hip joints.

reconstruction.[40–44] In addition, the MRF acquisition acquired a series of highly under-sampled acquisitions and hence are susceptible to aliasing artifacts. Several compressed sensing-based MRF reconstructions are known to reduce the effects of aliasing artifacts.[45–47]

MRF is also sensitive to motion artifacts due to the long scan time. The sliding window-based approach to correct for motion has also been proposed in previous studies.[48,49] The motion binning approach to correct for motion artifacts has also been demonstrated.[50]

Conclusion

Our preliminary study demonstrates the feasibility of a 3D-MRF sequence for the simultaneous acquisition of PD, T_1, T_2, $T_{1\rho}$, and ΔB_{1+} parameter maps of the articular cartilage of the bilateral hip joints in a single scan in healthy and mild hip OA patients.

Acknowledgments

This study was supported by National Institutes of Health (NIH) grants R01 AR076328, R01 AR076985, and R01-AR078308, performed under the Center of Advanced Imaging Innovation and Research (CAI2R) at NYU Grossman School of Medicine and NIBIB Biomedical Technology Resource Center (NIH P41 EB017183).

References

1. Pun S, Kumar D, Lane NE. Femoroacetabular impingement. Arthritis Rheumatol 2015;67(1):17-27.
2. Blankenbaker DG, Tuite MJ. MR imaging of early hip joint degeneration. Magn Reson Imaging Clin N Am 2011;19(2):365-378.
3. Su T, Chen GX, Yang L. Diagnosis and treatment of labral tear. Chin Med J (Engl) 2019;132(2):211-219.
4. McDevitt CA. Biochemistry of articular cartilage. Nature of proteoglycans and collagen of articular cartilage and their role in ageing and in osteoarthrosis. Ann Rheum Dis 1973;32(4):364-378.

5. Venn M, Maroudas A. Chemical composition and swelling of normal and osteoarthrotic femoral head cartilage. I. Chemical composition. Ann Rheum Dis 1977;36(2):121-129.
6. Cohen NP, Foster RJ, Mow VC. Composition and dynamics of articular cartilage: Structure, function, and maintaining healthy state. J Orthop Sports Phys Ther 1998;28(4):203-215.
7. Duvvuri U, Reddy R, Patel SD, Kaufman JH, Kneeland JB, Leigh JS. $T_{1\rho}$-relaxation in articular cartilage: Effects of enzymatic degradation. Magn Reson Med 1997;38(6):863-867.
8. Sophia Fox AJ, Bedi A, Rodeo SA. The basic science of articular cartilage: Structure, composition, and function. Sports Health 2009;1(6): 461-468.
9. Mosher TJ, Dardzinski BJ. Cartilage MRI T_2 relaxation time mapping: Overview and applications. Semin Musculoskelet Radiol 2004;8(4): 355-368.
10. Regatte RR, Akella SVS, Lonner JH, Kneeland JB, Reddy R. $T_{1\rho}$ relaxation mapping in human osteoarthritis (OA) cartilage: Comparison of $T_{1\rho}$ with T_2. J Magn Reson Imaging 2006;23(4):547-553.
11. Bittersohl B, Hosalkar HS, Kim Y, et al. T_1 assessment of hip joint cartilage following intra-articular gadolinium injection: A pilot study. Magn Reson Med 2010;64(4):1200-1207.
12. Dunn TC, Lu Y, Jin H, Ries MD, Majumdar S. T_2 relaxation time of cartilage at MR imaging: Comparison with severity of knee osteoarthritis. Radiology 2004;232(2):592-598.
13. Mosher TJ, Smith H, Dardzinski BJ, Schmithorst VJ, Smith MB. MR imaging and T_2 mapping of femoral cartilage. Am J Roentgenol 2001; 177(3):665-669.
14. Liess C, Lüsse S, Karger N, Heller M, Glüer CG. Detection of changes in cartilage water content using MRI T_2-mapping in vivo. Osteoarthr Cartil 2002;10(12):907-913.
15. Duvvuri U, Kudchodkar S, Reddy R, Leigh JS. $T_{1\rho}$ relaxation can assess longitudinal proteoglycan loss from articular cartilage in vitro. Osteoarthr Cartil 2002;10(11):838-844.
16. Stahl R, Luke A, Li X, et al. T_{1rho}, T_2 and focal knee cartilage abnormalities in physically active and sedentary healthy subjects versus early OA patients—A 3.0-Tesla MRI study. Eur Radiol 2009;19(1):132-143.
17. Lattanzi R, Glaser C, Mikheev AV, et al. A B_1-insensitive high resolution 2D T_1 mapping pulse sequence for dGEMRIC of the HIP at 3 Tesla. Magn Reson Med 2011;66(2):348-355.
18. Bashir A, Gray ML, Burstein D. Gd-DTPA^{2-} as a measure of cartilage degradation. Magn Reson Med 1996;36(5):665-673.
19. Iyad N, Ahmad S, Alkhatib SG, Hjouj M. Gadolinium contrast agents-challenges and opportunities of a multidisciplinary approach: Literature review. Eur J Radiol Open 2023;11:100503.
20. Nieminen MT, Töyräs J, Rieppo J, et al. Quantitative MR microscopy of enzymatically degraded articular cartilage. Magn Reson Med 2000; 43(5):676-681.
21. Nissi MJ, Rieppo J, Töyräs J, et al. T_2 relaxation time mapping reveals age- and species-related diversity of collagen network architecture in articular cartilage. Osteoarthr Cartil 2006;14(12):1265-1271.
22. Li X, Pai A, Blumenkrantz G, et al. Spatial distribution and relationship of $T_{1\rho}$ and T_2 relaxation times in knee cartilage with osteoarthritis. Magn Reson Med 2009;61(6):1310-1318.
23. Monga A, Singh D, de Moura HL, Zhang X, Zibetti MVW, Regatte RR. Emerging trends in magnetic resonance fingerprinting for quantitative biomedical imaging applications: A review. Bioengineering 2024; 11(3):236.
24. Kijowski R, Sharafi A, Zibetti MVW, Chang G, Cloos MA, Regatte RR. Age-dependent changes in knee cartilage T_1, T_2, and $T_{1\rho}$ simultaneously measured using MRI fingerprinting. J Magn Reson Imaging 2023;57(6):1805-1812.
25. Li Q, Cao X, Ye H, Liao C, He H, Zhong J. Ultrashort echo time magnetic resonance fingerprinting (UTE-MRF) for simultaneous quantification of long and ultrashort T_2 tissues. Magn Reson Med 2019;82(4): 1359-1372.
26. Cloos MA, Assländer J, Abbas B, et al. Rapid radial T_1 and T_2 mapping of the hip articular cartilage with magnetic resonance fingerprinting. J Magn Reson Imaging 2019;50(3):810-815.
27. Sharafi A, Zibetti MVW, Chang G, Cloos MA, Regatte RR. Simultaneous bilateral T_1, T_2, and $T_{1\rho}$ relaxation mapping of the hip joint with magnetic resonance fingerprinting. NMR Biomed 2022;35(5):e4651.
28. Menon RG, Monga A, Kijowski R, Regatte RR. Characterization of age-related and sex-related differences of relaxation parameters in the intervertebral disc using MR-fingerprinting. J Magn Reson Imaging 2023;59:1312-1324.
29. Sharafi A, Zibetti MVW, Chang G, Cloos M, Regatte RR. 3D magnetic resonance fingerprinting for rapid simultaneous T_1, T_2, and $T_{1\rho}$ volumetric mapping of human articular cartilage at 3 T. NMR Biomed 2022; 35(12):e4800.
30. Gram M, Seethaler M, Gensler D, Oberberger J, Jakob PM, Nordbeck P. Balanced spin-lock preparation for B_1-insensitive and B_0-insensitive quantification of the rotating frame relaxation time $T_{1\rho}$. Magn Reson Med 2021;85(5):2771-2780.
31. Weigel M. Extended phase graphs: Dephasing, RF pulses, and echoes – pure and simple. J Magn Reson Imaging 2015;41(2):266-295.
32. McGivney DF, Pierre E, Ma D, et al. SVD compression for magnetic resonance fingerprinting in the time domain. IEEE Trans Med Imaging 2014;33(12):2311-2322.
33. Zibetti MVW, Sharafi A, Regatte RR. Optimization of spin-lock times in $T_{1\rho}$ mapping of knee cartilage: Cramér-Rao bounds versus matched sampling-fitting. Magn Reson Med 2022;87(3):1418-1434.
34. Sharafi A, Chang G, Regatte RR. Biexponential T_2 relaxation estimation of human knee cartilage in vivo at 3T. J Magn Reson Imaging 2018; 47(3):809-819.
35. Stupic KF, Ainslie M, Boss MA, et al. A standard system phantom for magnetic resonance imaging. Magn Reson Med 2021;86(3):1194-1211.
36. Lee S, Nardo L, Kumar D, et al. Scoring hip osteoarthritis with MRI (SHOMRI): A whole joint osteoarthritis evaluation system. J Magn Reson Imaging 2015;41(6):1549-1557.
37. Anwander H, Rakhra KS, Melkus G, Beaulé PE. $T_{1\rho}$ hip cartilage mapping in assessing patients with cam morphology: How can we optimize the regions of interest? Clin Orthop Relat Res 2017;475(4):1066-1075.
38. Wyatt C, Kumar D, Subburaj K, et al. Cartilage $T_{1\rho}$ and T_2 relaxation times in patients with mild-to-moderate radiographic hip osteoarthritis. Arthritis Rheumatol 2015;67(6):1548-1556.
39. Subburaj K, Valentinitsch A, Dillon AB, et al. Regional variations in MR relaxation of hip joint cartilage in subjects with and without femoralacetabular impingement. Magn Reson Imaging 2013;31(7): 1129-1136.
40. Barbieri M, Lee PK, Brizi L, et al. Circumventing the curse of dimensionality in magnetic resonance fingerprinting through a deep learning approach. NMR Biomed 2022;35(4):e4670.
41. Cabini RF, Barzaghi L, Cicolari D, et al. Fast deep learning reconstruction techniques for preclinical magnetic resonance fingerprinting. NMR Biomed 2024;37(1):e5028.
42. Fang Z, Chen Y, Hung SC, Zhang X, Lin W, Shen D. Submillimeter MR fingerprinting using deep learning–based tissue quantification. Magn Reson Med 2020;84(2):579-591.
43. Cohen O, Zhu B, Rosen MS. MR fingerprinting Deep RecOnstruction NEtwork (DRONE). Magn Reson Med 2018;80(3):885-894.
44. Wang Z, Zhang J, Cui D, et al. Magnetic resonance fingerprinting using a fast dictionary searching algorithm: MRF-ZOOM. IEEE Trans Biomed Eng 2019;66(6):1526-1535.
45. Zhao B, Setsompop K, Adalsteinsson E, et al. Improved magnetic resonance fingerprinting reconstruction with low-rank and subspace modeling. Magn Reson Med 2018;79(2):933-942.
46. Zhao B. Model-based iterative reconstruction for magnetic resonance fingerprinting. *2015 IEEE international conference on image processing (ICIP).* Canada: IEEE; 2015. p 3392-3396. https://doi.org/10.1109/ICIP.2015.7351433

47. Nagtegaal M, Koken P, Amthor T, Doneva M. Fast multi-component analysis using a joint sparsity constraint for MR fingerprinting. Magn Reson Med 2020;83(2):521-534.

48. Marriott A, Rioux J, Brewer K. Nonuniform sliding-window reconstruction for accelerated dual contrast agent quantification with MR fingerprinting. Magn Reson Mater Phys Biol Med 2024;37(2):273-282.

49. Cao X, Liao C, Wang Z, et al. Robust sliding-window reconstruction for accelerating the acquisition of MR fingerprinting. Magn Reson Med 2017;78(4):1579-1588.

50. Cruz G, Qi H, Jaubert O, et al. Generalized low-rank nonrigid motion-corrected reconstruction for MR fingerprinting. Magn Reson Med 2022; 87(2):746-763.